



Universiteit
Leiden
The Netherlands

Patient-specific in-vivo QA in MRGRT: 3D EPID dosimetry for the Unity MR-linac

Torres Xirau, I.

Citation

Torres Xirau, I. (2020, September 15). *Patient-specific in-vivo QA in MRGRT: 3D EPID dosimetry for the Unity MR-linac*. Retrieved from <https://hdl.handle.net/1887/136754>

Version: Publisher's Version

License: [Licence agreement concerning inclusion of doctoral thesis in the Institutional Repository of the University of Leiden](#)

Downloaded from: <https://hdl.handle.net/1887/136754>

Note: To cite this publication please use the final published version (if applicable).

Cover Page



Universiteit Leiden

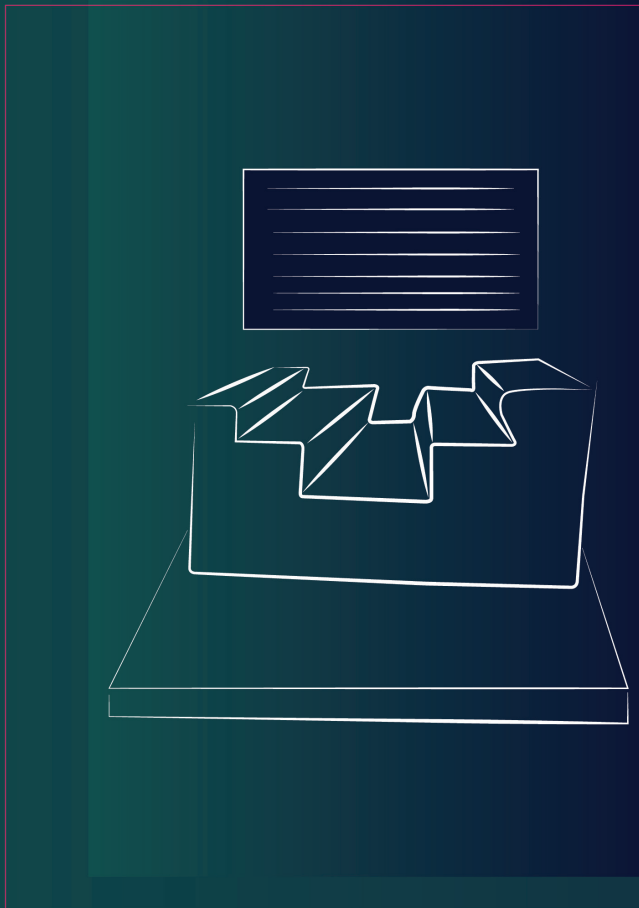


The handle <http://hdl.handle.net/1887/136754> holds various files of this Leiden University dissertation.

Author: Torres Xirau, I.

Title: Patient-specific in-vivo QA in MRGRT: 3D EPID dosimetry for the Unity MR-linac

Issue Date: 2020-09-15



2.

A BACK-PROJECTION ALGORITHM IN THE PRESENCE OF AN EXTRA ATTENUATING MEDIUM: TOWARDS EPID DOSIMETRY FOR THE MR-LINAC

**I Torres-Xirau
I Olaciregui-Ruiz
R A Rozendaal
P González
B J Mijnheer
J-J Sonke
U A van der Heide
A Mans**

Department of Radiation Oncology,
The Netherlands Cancer Institute–Antoni van Leeuwenhoek Hospital,
Plesmanlaan 121, 1066 CX Amsterdam, The Netherlands

*Physics in Medicine & Biology, Volume 62, Number 15
Published 17 July 2017 • © 2017 Institute of Physics and Engineering in Medicine*

Abstract

In external beam radiotherapy, Electronic Portal Imaging Devices (EPIDs) are frequently used for pre-treatment and for *in vivo* dose verification. Currently, various MR-guided radiotherapy systems are being developed and clinically implemented. Independent dosimetric verification is highly desirable. For this purpose, we adapted our EPID-based dose verification system for use with the MR-Linac combination developed by Elekta in cooperation with UMC Utrecht and Philips.

In this study we extended our back-projection method to cope with the presence of an extra attenuating medium between the patient and the EPID. Experiments were performed at a conventional linac, using an aluminum mock-up of the MRI scanner housing between the phantom and the EPID. For a 10 cm square field, the attenuation by the mock-up was 72%, while 16% of the remaining EPID signal resulted from scattered radiation.

58 IMRT fields were delivered to a 20 cm slab phantom with and without the mock-up. EPID reconstructed dose distributions were compared to planned dose distributions using the γ -evaluation method (global, 3%, 3mm). In our adapted back-projection algorithm the averaged γ_{mean} was 0.27 ± 0.06 , while in the conventional was 0.28 ± 0.06 . Dose profiles of several square fields reconstructed with our adapted algorithm showed excellent agreement when compared to TPS.

Keywords: EPID dosimetry, MR-Linac, patient-specific, pre-treatment, *in vivo*, verification, IMRT

2.1. Introduction

Image-guided radiotherapy strives to correct for tumor misalignments derived from setup error, posture change, organ motion, etc., which may otherwise lead to suboptimal treatments. However, deformation and anatomical changes related to treatment response are typically not included in the regular IGRT workflow. Moreover, the in-room image quality is not always sufficient to visualize the tumor and relevant organs-at-risk. Hence, several groups are currently investigating the potential of radiotherapy treatment systems with integrated MR imaging modality. One example is the MRIdian System (ViewRay, Inc., Oakwood Village, OH), which integrates three Cobalt-60 heads with a 0.35-T split MRI system¹⁰⁶. The Linac-MR (Cross Cancer Institute, Edmonton AB, Canada) consists of an isocentrically rotating 6 MV linac with a biplanar 0.5-T MRI in the transverse plane allowing perpendicular and parallel irradiation to the magnetic field^{107,108}. The Australian MRI-Linac system connects a specifically designed 1-T open-bore MRI with a 6-MV linac¹⁰⁹. The MRI-linac program investigated by Siemens places a 6MV linac in a ring around a conventional MRI magnet¹¹⁰. Another initiative couples a 1.5-T, diagnostic quality, magnetic resonance imaging with a linear accelerator (Elekta AB, Stockholm, Sweden in cooperation with UMC Utrecht, The Netherlands and Philips, Best, The Netherlands)⁹². When combined with fast (re)contouring and (re)planning software, MRI-based online adaptive strategies are expected to become feasible⁹⁴. The Elekta MR-Linac is currently being installed in our institute.

The high complexity of online treatment adaptation makes independent dosimetric verification in the MR-Linac system highly desirable. Alternative quality assurance techniques involving the use of the linac log files and MRI 3D patient anatomy could allow identification of potential errors in data transfer, dose delivery, patient set-up, and

changes in patient anatomy, but not in dose calculation or MLC calibration¹⁰⁵ and not in real-time. The aim of transit EPID dosimetry at the MR-Linac is to verify the delivered 3D dose to the patient, hence providing an independent real-time verification of the entire treatment chain.

Several studies of dose-response characteristics have shown that a-Si EPIDs are suitable for dose verification^{111, 112, 113, 114, 115}. It was demonstrated⁹³ in addition that the portal imager integrated in the MR-Linac is able to acquire EPID images simultaneously to MRI imaging. Our back-projection algorithm has been described previously in detail^{70, 58} and is used to perform *in vivo* EPID dosimetry routinely for almost all IMRT and VMAT as well as 3D conformal radiotherapy treatments in our clinic since January 2008⁹⁰.

The geometry of the MR-Linac poses several challenges for EPID based dosimetry:

- The presence of the MRI housing between the patient and the EPID serves as a non-uniform attenuating medium and as a source of scattered radiation. Furthermore, it alters the photon energy spectrum of the beam.
- The 1.5T magnetic field affects the dose deposition in the patient (or phantom)^{91, 117}
- The small magnetic field at the EPID location possibly influences the dose-response characteristics of the EPID⁹³.

As a first step towards portal dosimetry in the MR-Linac, the purpose of this study was to correct for the scattering and attenuating effects in the EPID images caused by a step-shaped extra attenuating medium mimicking the MRI housing, and to back-project the corrected portal dose images into the patient's geometry.

The use of such an MRI scanner mock-up at a conventional linac is

an excellent opportunity to investigate the first of the aforementioned challenges separately, in a controlled fashion, without the need for solving the other challenges simultaneously. The influence of the magnetic field on the dose delivery both in the patient/phantom inside the bore of the MR-Linac and at the EPID level is beyond the scope of this study, but will be subject of future work.

2.2. Materials and Methods

2.2.1 Conventional back-projection algorithm

In summary, our in-house technique^{58,70} requires seven steps to reconstruct the dose in the phantom or patient from the EPID images acquired during treatment. These seven steps account for:

- i. Pixel sensitivity matrix (S_{ij} Matrix) which corrects for the variation in individual pixel sensitivity and in the off-axis differential photon energy⁴⁶.
- ii. Dose response of the EPID.
- iii. Lateral scatter within the EPID.
- iv. Scatter from the phantom or patient to the EPID.
- v. Attenuation of the beam by the phantom or patient.
- vi. Scatter within the phantom or patient.
- vii. Build-up effects.

In the conventional algorithm, the dose measured at the EPID level is determined after step 3.

2.2.2 Adapted back-projection algorithm

In the MR-Linac, before reaching the EPID, the

beam is affected by the presence of the MRI scanner. A sketch of the geometry of the conventional linac and the MR-Linac is given in **Figure 2.1**. The MRI housing acts as the main source of scatter in portal images, attenuates the beam and modifies its photon energy spectrum. In this work the measured portal dose behind the MRI scanner, PD_{ij}^{MRI} is corrected for the aforementioned effects, determining $PD_{ij}^{MRI,corrected}$.

In other words, $PD_{ij}^{MRI,corrected}$ estimates what would be the dose measured at the EPID level in the absence of the MRI housing, taking as input images that have been measured behind the the MRI housing.

The index pair ij refers to a pixel of the EPID at position (i,j) .

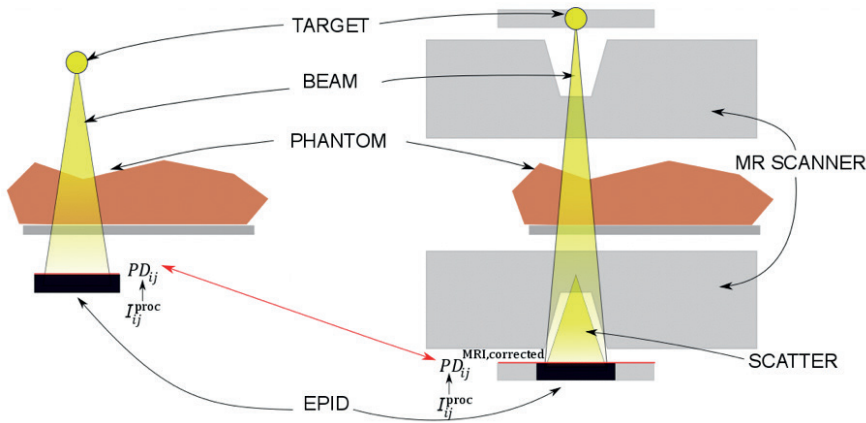


Figure 2.1: Cross section of the conventional Linac (left) and the MR-Linac (right) geometry. After the portal images I_{ij}^{proc} are processed, the portal dose PD_{ij} on the left corresponds to the portal dose corrected $PD_{ij}^{MRI,corrected}$ on the right and the back-projection is continued as in the conventional method.

To achieve this, the 3rd step of our conventional algorithm (portal dose determination) has been expanded to:

- correction for lateral scatter within the EPID (step 3 in conventional algorithm), obtaining the portal dose behind the MR-Linac, PD_{ij}^{MRI} ,
- subtraction of that part of the portal dose due to scatter from the MRI housing to the EPID, $Sc_{ij}^{MRI \rightarrow EPID}$, obtaining $PD_{ij}^{MRI,ScatCorr}$,
- correction for the extra attenuation in $PD_{ij}^{MRI,ScatCorr}$ and changes in energy spectrum due to the MRI housing, obtaining $PD_{ij}^{MRI,ScatCorr}$.

After the effects caused by the MRI scanner on the EPID images are corrected, the resulting the portal dose MRI-corrected, $PD_{ij}^{MRI,Corrected}$, is used in the remaining steps of the algorithm, which is identical to the conventional version.

In what follows, two specific configurations are used:

- MRI geometry: in the MR-Linac the beam always traverses the MRI scanner. I_{ij}^{MRI} images can be obtained with patient $I_{ij}^{MRI,patient}$, or without patient $I_{ij}^{MRI,open}$. Along the description of the fitting algorithm and the commissioning of the model, “open” or “patient” are specified, unless the expression is valid for both set-ups.
- Empty geometry: in this case the MRI scanner, patient and couch are not present. Although this set-up is unrealistic in the clinical/actual set-up, the current calibration procedure of our transmission-based algorithm requires a set of I_{ij}^{empty} images to determine the parameters of the MRI \rightarrow EPID scatter kernel.

A. Subtraction of radiation scattered from the MRI housing to the EPID

The scattered radiation from the MRI scanner to the EPID is treated in the same way as the scattered radiation from the patient reaching the EPID in our conventional algorithm because of the similarity of these cases. The scatter is modeled as a convolution between the portal dose image and a scatter kernel, and the kernel parameters are determined by a fitting process described below.

The portal dose behind the MRI scanner PD_{ij}^{MRI} , includes the component $Sc_{ij}^{MRI \rightarrow EPID}$ due to scatter from the MRI scanner to the EPID.

$$PD_{ij}^{MRI} = PD_{ij}^{MRI, ScatCorr} + Sc_{ij}^{MRI \rightarrow EPID}, \quad (1)$$

where $PD_{ij}^{MRI, ScatCorr}$ represents the portal dose of radiation reaching the EPID as if the scatter from the MRI scanner was not present.

The portal dose in the conventional algorithm (i.e., after step 3) PD_{ij} , corresponds to a processed EPID image containing dose information and is calculated as:

$$PD_{ij} = I_{ij}^{proc} \cdot S_{ij} \cdot Dr \otimes^{-1} K1_{\square} \otimes K2_{\square} \quad (2)$$

where I_{ij}^{proc} is the time-integrated EPID image processed for the dark field, flood field and bad pixels¹¹⁹. S_{ij} is the pixel sensitivity matrix, Dr is the dose response of the EPID, and $K1_{\square}$ and $K2_{\square}$ are kernels correcting for the lateral scatter within the EPID. $K1_{\square}$ accounts for the lateral scatter within the EPID based on a central axis parametric fit, and $K2_{\square}$ is a blurring kernel such that the EPID images

agree with the off-axis data from the ionization chamber, affecting mainly the penumbra region ⁷⁰. The aim of the convolution with $K2$ is to match better the penumbras while maintaining the on-axis agreement obtained by $K1$.

Note that fluence is not determined in our semi-empirical algorithm.

Convolution and deconvolution were performed in frequency domain using the fast Fourier transform in two dimensions and the calculation time to process the EPID image after acquisition was of the order of 10 ms.

Unlike in the conventional linac, in the MR-Linac, a large scatter contribution from the MRI housing to the EPID exists, together with a step-shaped attenuation and differences in photon beam energy spectra. Therefore, the EPID responds differently behind the MRI scanner, and both PD_{ij}^{empty} and PD_{ij}^{MRI} portal dose images require separate calibration data-sets and have to be calculated with different parameters:

$$PD_{ij}^{MRI} = I_{ij}^{MRI} \cdot S_{ij}^{MRI} \cdot Dr_{ij}^{MRI} \otimes^{-1} K1_{ij}^{MRI} \otimes K2_{ij}^{MRI} \quad (3)$$

$$PD_{ij}^{empty} = I_{ij}^{empty} \cdot S_{ij}^{empty} \cdot Dr_{ij}^{empty} \otimes^{-1} K1_{ij}^{empty} \otimes K2_{ij}^{empty} \quad (4)$$

The transmission of the beam through the MRI scanner is now defined as the ratio between “MRI-open” (3) and “empty” (4) portal dose images

$$T_{ij}^{total,MRI} = \frac{PD_{ij}^{MRI,open}}{PD_{ij}^{empty}} \quad (5)$$

and will be called MRI total transmission. By using (1) it can be

separated into a primary and a scatter component,

$$T_{ij}^{total,MRI} = T_{ij}^{primary,MRI} + \frac{Sc_{ij}^{MRI \rightarrow EPID}}{PD_{ij}^{empty}} \quad (6)$$

where $T_{ij}^{primary,MRI}$ denotes the transmission of the primary photons measured with the EPID.

The scatter from the MRI to the EPID and consequently the total transmission $T_{ij}^{total,MRI}$ in (6) are field size dependent¹²⁰, while the primary transmission $T_{ij}^{primary,MRI}$ is by definition field size independent. To determine the scatter component to the portal dose, the total transmission $T_{ij}^{total,MRI}$, is experimentally determined with (5) as a function of field size fs , by irradiating the EPID with and without the mock-up of the MRI scanner with square fields of different sizes. In the limit of zero field size, the total transmission $T_{ij}^{total,MRI}$ equals the primary transmission $T_{ij}^{primary,MRI}$ as the scatter from the MRI scanner reaching the EPID tends to zero. On-axis values of the total transmission, $\langle T_{ij}^{total,MRI} \rangle_{cROI}$, are plotted as a function of field area, fs^2 , and the limit to zero field area is calculated by parametrizing the curve of $\langle T_{ij}^{total,MRI} \rangle_{cROI}$. The brackets $\langle \rangle_{cROI}$ represent the average over a small central region of interest (cROI) of the EPID at the central axis.

$$\langle T_{ij}^{primary,MRI} \rangle_{cROI} \approx \lim_{fs \rightarrow 0} [\langle T_{ij}^{total,MRI}(fs^2) \rangle_{cROI}] \quad (7)$$

Since at small air-gaps the transmission is no longer linearly related with field area¹²⁰, a second-order polynomial was used to parametrize the $\langle T_{ij}^{total,MRI} \rangle_{cROI}$ for the 15cm air-gap used in our set-up (see section 2.4), and the constant $\langle T_{ij}^{primary,MRI} \rangle_{cROI}$ is obtained using (7).

The scatter from the MRI scanner to the EPID is modeled in the portal

dose as a convolution of the MRI- open portal dose image with a scatter kernel $K_{ij}^{MRI \rightarrow EPID}$,

$$S_{C_{ij}}^{MRI \rightarrow EPID} = PD_{ij}^{MRI,open} \otimes K_{ij}^{MRI \rightarrow EPID} \quad (8)$$

Based on the iterative approach to determine the scatter from the patient to the EPID suggested in^{121, 122}, we investigated the use of a similar iterative approach using the scatter corrected MRI-open portal dose $PD_{ij}^{MRI,open,ScatCorr}$ in (8) instead of the MRI-open portal dose $PD_{ij}^{MRI,open}$. However, preliminary results showed that the MRI-open portal dose itself appeared to be a good approximation, as the fitting results after 6 iterations improved only 0.025% the Euclidean distance between $\langle T_{ij}^{primary,MRI} \rangle_{cROI}$ and $\langle T_{ij}^{primary,MRI}(fS; \sigma_{MRI}^2, c_{MRI}) \rangle_{cROI}$. In this work, a gaussian filter was used as a scatter kernel,

$$K_{ij}^{MRI \rightarrow EPID} = \frac{c_{MRI}}{2\pi\sigma_{MRI}^2} \exp\left(-\frac{r_{ij}^2}{2\sigma_{MRI}^2}\right), \quad (9)$$

where r_{ij} is the distance of a pixel ij from the central axis.

In order to determine the parameters σ_{MRI}^2 and c_{MRI} , the primary transmission $\langle T_{ij}^{primary,MRI}(fS; \sigma_{MRI}^2, c_{MRI}) \rangle_{cROI}$, is calculated for different field sizes using (6) (and (8), (9) to introduce σ_{MRI}^2 and c_{MRI}) and fitted for all field sizes to the zero-field-size limit of the total transmission calculated in (7)), $\langle T_{ij}^{primary,MRI} \rangle_{cROI}$ by:

$$\min_{\sigma_{MRI}^2, c_{MRI}} \left(\langle T_{ij}^{primary,MRI} \rangle_{cROI} - \langle T_{ij}^{primary,MRI}(fS; \sigma_{MRI}^2, c_{MRI}) \rangle_{cROI} \right) \quad (10)$$

where $\min()$ is a minimization function, and the aim is to fulfill the field size independence of the $\langle T_{ij}^{primary,MRI} \rangle_{cROI}$ with the correct parameters

determination.

B. Correction for the MRI housing attenuation

An experimentally determined primary transmission 2D map is applied to the scatter corrected MRI-open image, $PD_{ij}^{MRI,open,ScatCorr}$, to account for the attenuation and beam hardening in the MRI housing.

This primary transmission map is defined as the ratio between the portal dose MRI-open image corrected or the scatter $PD_{ij}^{MRI,open,ScatCorr}$, and an empty portal dose image PD_{ij}^{empty} for a large square field ($26 \times 26 \text{ cm}^2$):

$$Tmap_{ij} = \frac{PD_{ij}^{MRI,open,26 \times 26} - Sc_{ij}^{MRI \rightarrow EPID}}{PD_{ij}^{empty,26 \times 26}} \quad (11)$$

The final portal dose corrected for the effects of the MRI scanner

$PD_{ij}^{MRI,corrected}$ can be expressed as:

$$PD_{ij}^{MRI,Corrected} = \frac{PD_{ij}^{MRI,ScatCorr}}{Tmap_{ij}} \quad (12)$$

2.2.3 Commissioning data

To support the additional two steps in our dose reconstruction engine, new measurements had to be added to the regular set of commissioning data, which is summarized in¹²³. Also, the reconstruction dose engine had to be adapted in the commissioning and in the verification software. The required complete new set of commissioning data consists of EPID images, water tank measurements and reference ionization chamber values for each configuration (“MRI-phantom”, “MRI-open” and “empty”) irradiated with square fields of increasing size (2×2 - 26×26

cm²) and is summarized in **Table 2.1**.

Commissioning measurements for the “empty” configuration were acquired on a regular 6 MV photon beam of an SL20i linear accelerator with flattening filter, without the aluminum structure in place, while the set-up for the rest of the measurements included the mock-up between isocenter and EPID, and a slab phantom only when indicated.

Table 2.1: Measurements required for commissioning of the model. The required extra measurement series (with respect to the conventional model) that are used for the determination of the scatter from the MRI and the attenuation map of our adapted method, are marked with (*). The commissioning measurements that determine the rest of the parameters are acquired similarly to as in the conventional method, considering the “MR” as the standard configuration in the MR-Linac.

Measurement	Configuration	Comment	Equipment	Phantom (cm ³)	Field Size (cm ²)
1. S_{ij} matrix	Empty*	To measure the relative sensitivity over the entire EPID	a) Ionization chamber in a mini-phantom in an empty water tank b) 2 EPID images		26x26
2. Field size series	Empty*	Measure and acquire at the EPID level (160 cm SSD)	a) Ionization chamber in a mini-phantom b) EPID images		Series 2x2- 20x20

3. S_{ij} matrix	MR-open	To measure the relative sensitivity over the entire EPID behind the MRI	a) Ionization chamber in a mini-phantom in an empty water tank b) 2 EPID images		26x26
4. Field size series	MR-open	Measure and acquire at the EPID level (160 cm SSD)	a) Ionization chamber in a mini-phantom b) EPID images		Series 2x2- 20x20
5. Field size series	MR-phantom	Constant phantom thickness, varying field size	a) Ionization chamber at isocenter in slab phantom b) EPID images	30x30x20 slab	Series 2x2- 20x20
6. Thickness series	MR-phantom	Constant field size, varying phantom thickness	a) Ionization chamber at isocenter in slab phantom b) EPID images	Series 30x30x4-40	10x10
7. Build up	MR-phantom	Constant field size, constant phantom thickness	Ionization chamber in a slab phantom at different depths	30x30x20	10x10

2.2.4 MRI scanner surrogate

To quantify the performance of our adapted algorithm, an experimental set-up was built in a conventional linac, consisting of an aluminum structure positioned between the phantom and the EPID, mimicking the geometry of the exit beam side of the MRI scanner. We define the axis of an EPID image parallel to the gun target direction as Y, and the axis perpendicular to it, X.

In the magnet of the MR-Linac, the central 15 cm in the Y direction is free of coils and shimming hardware in order to minimize beam attenuation and obtain homogeneous transmission. This 15 cm gap allows a maximum irradiation field of 22 cm in the cranial-caudal direction at the isocenter. However, for field sizes larger than 10 cm at the isocenter, the exit beam exceeds the 15 cm of the gap at the exit side and therefore, EPID images suffer from an extra attenuation at the edges in the Y direction as can be seen from **Figure 2.2.a,b**.

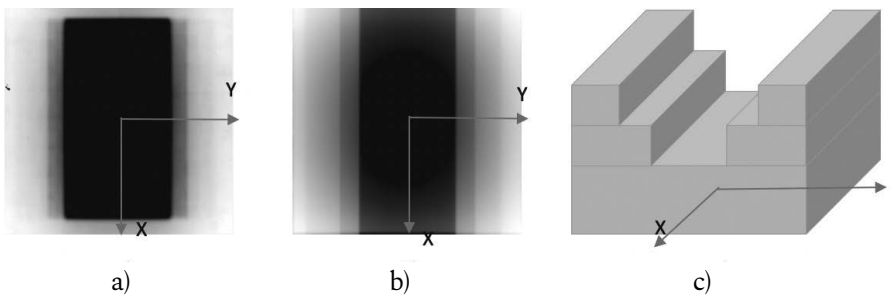


Figure 2.2: a) EPID images of a large field size acquired at the second MR-Linac prototype at the UMC Utrecht; b) EPID images of a large field size acquired at our institute with the aluminum structure; c) Schematic drawing of the aluminum structure used at our institute to mimic the effect of the MRI scanner.

To mimic this configuration at a conventional linac, an aluminum MRI-scanner mock-up was designed making use of the available information in literature. As reported^{124, 126, 93}, the irradiation beam travels through the equivalent of approximately 12 cm of aluminum

on-axis, hence an aluminum plate of 12 cm thickness at 15 cm distance from the EPID was used. Off-axis, the larger thickness of the magnet in the Y direction was mimicked by thicker aluminum blocks of 18 cm and 21 cm (**Figure 2.2.c**).

The presence of the MRI scanner between source and patient was not included in our mock-up since the effects it causes are not to be taken care of by our back-projection dosimetry model. To validate this choice, an experiment was performed with an extra structure of aluminum between the source and the isocenter. EPID images were acquired in a conventional linac with the aluminum structure between the isocenter and the EPID, both with and without 12cm extra of aluminum between the source and the isocenter. EPID readouts (normalized to the 10x10 cm² field size) were compared. For further experiments, no aluminum mock-up was used between source and isocenter.

2.2.5 Accelerator and EPID

All measurements in our institute were performed using a 6 MV photon beam of an SL20i linear accelerator with flattening filter (Elekta AB, Stockholm, Sweden), equipped with a multileaf collimator (MLC) of 80 leaves with a projected leaf width of 1 cm at the isocenter, which is located 100cm from the target. A PerkinElmer RID 1680 AL5/Elekta iViewGT a-Si EPID was used for all measurements. Images were acquired using in-house developed software^{114, 119}.

2.2.6 Square field and test field validation

To validate our method off-axis, EPID images acquired behind the phantom and the aluminum structure during the commissioning were back-projected using our adapted method into a 20 cm slab phantom for different square field sizes (2x2, 3x3, 5x5, 10x10, 15x15, 20x20 cm²).

A test field presenting a more complex geometry was included in the validation. The test field contained areas with signal coming from a single open MLC leaf (with adjacent leaves blocking radiation), another area with signal from two leaves only, and so on, resembling characteristics of an IMRT beam.

Cross-plane dose profiles and depth-dose curves were obtained and compared to the planned dose distributions and to measured curves in a water tank by an ultra-small detector: the microDiamond detector (PTW, Freiburg, Germany). 2D dose distributions reconstructed at the isocenter were compared to the planned dose distributions by γ -evaluation (global 3%, 3mm). For visual inspection, a 2D signed γ -evaluation is used in our clinic to indicate under-dosage or over-dosage when compared to the TPS.

2.2.7 IMRT plans and Treatment Planning System (TPS)

58 beams of 10 IMRT plans (5 tumor sites: lung, H&N, rectum, brain, breast) were included in this study. The plans were calculated for a step-and-shoot IMRT technique irradiating a 20 cm thick slab phantom, using 6 MV photon beams, with 2 to 7 segments per beam, with the beam angle set to 0° . Dose distributions were optimized in Pinnacle Version 9.8 (Philips Medical Systems, Eindhoven, The Netherlands). The treatments were randomly selected and their field sizes in the Y direction ranged from 7 to 17 cm. 2D dose distributions reconstructed at the isocenter were compared to the TPS dose distributions by means of γ -analysis (global 3%, 3mm) and the ROI of the γ -analysis was set to all pixels receiving more than 20% of the per-beam maximum dose.

To test the performance of our algorithm at different depths, 2D dose distributions reconstructed with our adapted algorithm were compared to the TPS for a 5-field Lung IMRT treatment on a 20 cm slab phantom by means of γ -analysis (global 3%, 3mm) at isocenter plane, and planes

5cm below and above that plane. The X and Y profiles obtained from the reconstructed dose distributions at the three depths were compared to the TPS profiles by visual inspection.

2.3 Results

2.3.1 EPID readouts with and without extra aluminum plate between source and isocenter

Figure 2.3 shows EPID output factors acquired with the aluminum mock-up between the isocenter and the EPID, both with and without a mock-up between the source and the isocenter. The curves show similar behavior, differences ranged from -3% to +3% for 3x3 cm² and 20x20 cm² fields respectively.

This indicates that scatter from the upper part of the MRI housing does not have a significant contribution in the EPID images.

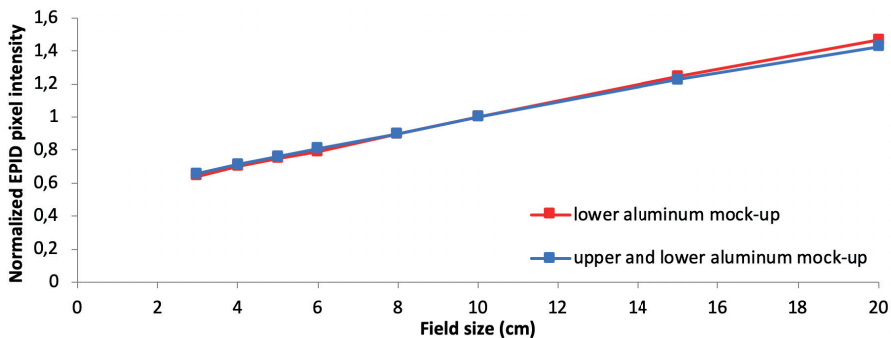


Figure 2.3: Central pixel values of EPID images for increasing square field sizes (3x3 - 20x20 cm²) normalized to the 10x10 cm² field size, acquired in a conventional linac both with the aluminum mock-up mimicking the effects of the upper and lower part of the MRI housing (blue), and only the lower part (red).

2.3.2 Magnitude of the corrections:

A quantitative description of the additional corrections applied to the portal dose measured by the EPID is reported for a 10x10 cm² field irradiating a 20 cm thick slab phantom. The scattered radiation from the aluminum mock-up reaching the EPID contributes to 16% of the measured EPID dose on-axis, which we successfully subtracted from the total portal dose using (1) as explained in section 2.2.2.A. The attenuation of the primary photons measured with the EPID as defined in (6), of the aluminum mock-up on-axis for the 6MV beam is 72%.

2.3.3 Square fields and test field validation:

In **Table 2.2** the 2-D γ -evaluation results comparing reconstructed dose distributions from back-projected EPID images acquired behind the aluminum structure to TPS dose distributions are presented for various square field sizes.

Table 2.2: Two-dimensional γ -evaluation for increasing square field sizes of a 6 MV photon beam comparing the reconstructed EPID midplane dose at 10 cm depth in a 20 cm thick polystyrene slab phantom at an SSD of 90 cm to the planned dose distribution by the TPS.

Field size (cm ²)	2x2	3x3	5x5	10x10	15x15	20x20
γ -evaluation						
γ_{mean}	0.38	0.38	0.33	0.27	0.26	0.22
$\gamma_{1\%}$	0.80	0.82	0.81	0.75	0.79	0.67
$\%_{\gamma \leq 1}$	100	100	100	100	99.9	100
$\Delta Dose_{iso}$	-0.7%	1.6%	-0.6%	0.2%	0.7%	0.8%

In **Figure 2.4.a,b**, X and Y dose profiles of square fields of different sizes from the TPS are shown respectively, together with dose profiles reconstructed from EPID images acquired behind the aluminum structure and also to dose profiles measured with a microDiamond detector. The X profile of the described test field is also shown in **Figure 2.4.c** for the microDiamond detector, the planned dose distribution, and for the EPID-derived dose distribution.

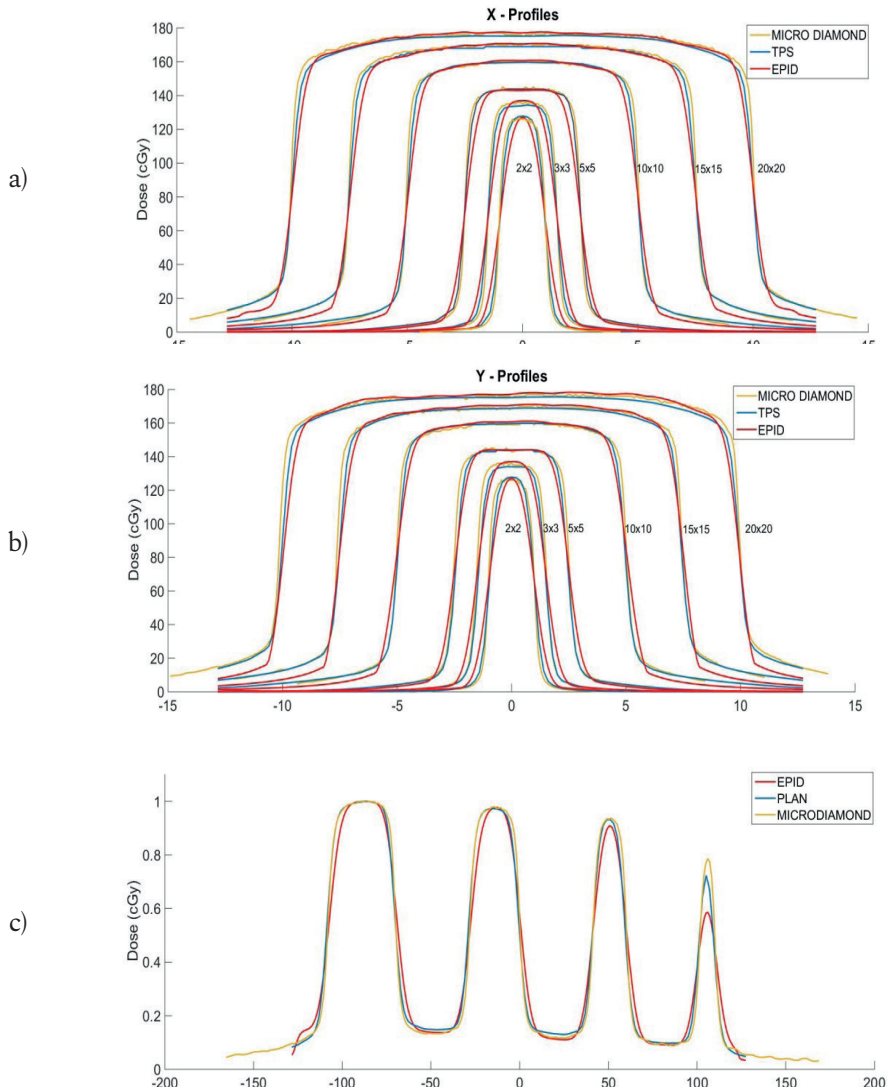


Figure 2.4: a,b) X and Y lateral profiles from the reconstructed EPID midplane dose at 10 cm depth for 6 MV photon beams of different square field sizes irradiating to a 20 cm thick slab. In blue, the X and Y profiles calculated by the treatment planning system at 10 cm depth. In yellow, measured dose profiles by a microDiamond detector in a water tank at the same depth; c) EPID, TPS and microDiamond detector curves of the lateral X profile of the described test field.

In **Figure 2.5** the depth-dose curve obtained from the EPID back-projected dose distribution is compared to TPS data and to the microDiamond detector measured curve for the 10x10 cm² square field.

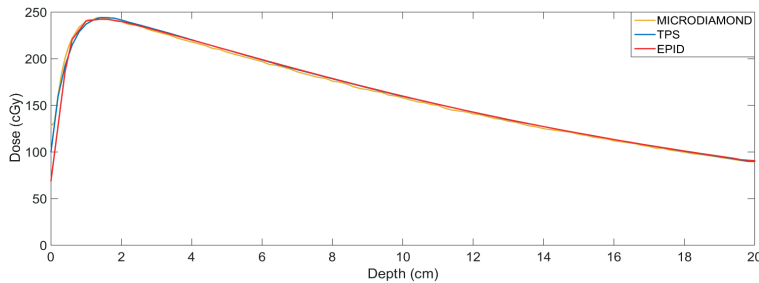





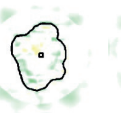
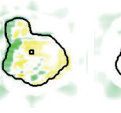


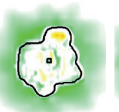
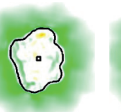
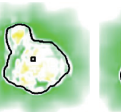

Figure 2.5: Comparison between depth-dose curves along the central beam axis through the isocenter for a 10x10 cm² field of a 6 MV photon beam irradiating a 20 cm thick slab phantom, taken from the reconstructed 3D dose distribution using EPID images behind the aluminum structure (blue), the planned TPS dose distribution (red), and the microDiamond measured curve (yellow).

When compared to the TPS, 96% of the points of the EPID curve showed deviations smaller than 2% and those points having larger deviations were situated at depths smaller than 0.4 cm and at depths larger than 19.5 cm. When compared to the microDiamond, 97% of the points of the EPID curve showed deviations smaller than 2% and those points having larger deviations were situated at depths smaller than 0.6 cm and at depths larger than 19.5 cm.

2.3.4 Reconstruction of IMRT plans:

As an example, **Table 3** presents the 2-D γ evaluation (3%, 3mm) at the isocenter plane of a 6 MV lung IMRT plan consisting of 5 beams delivered to a 20 cm thick slab phantom.

Table 2.3: 2D γ -evaluation of EPID reconstructed dose distributions compared to the TPS at the isocenter for a 5-field IMRT plan delivered to a 20 cm thick polystyrene phantom. The top row uses the conventional back-projection algorithm and the bottom row the MRI-adapted back-projection algorithm for the situation without and with the bottom aluminum structure, respectively.

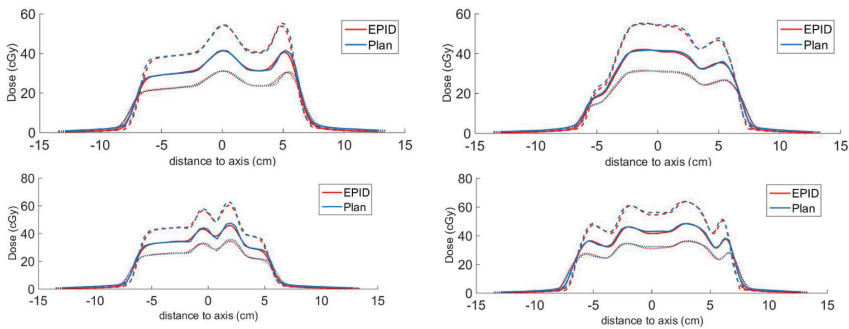
						
Without aluminum structure						Δ Dose isocentre
γ_{mean}	0.34	0.20	0.17	0.34	0.21	-0.5%
$\gamma_{1\%}$	0.89	0.61	0.51	0.85	0.70	
$\% \gamma_{\leq 1}$	99.7	100.0	100.0	99.7	99.8	
With bottom aluminum structure						Δ Dose isocentre
γ_{mean}	0.24	0.24	0.19	0.23	0.18	-0.6%
$\gamma_{1\%}$	0.69	1.03	0.71	0.86	0.58	
$\% \gamma_{\leq 1}$	100	98.6	99.6	99.7	100	

A 2D γ -evaluation per beam of the same treatment was performed at isocenter+5cm and isocenter-5cm with the aluminum mock-up between the phantom and the EPID and using our adapted back-projection algorithm. The γ results when compared to the TPS are presented in **Table 2.4:**

Table 2.4: 2D γ -evaluation of EPID reconstructed and planned dose distributions at 5 cm above and below the isocenter plane, for a 5-field IMRT plan delivered to a 20 cm thick polystyrene phantom.

Isoc +5cm						Δ Dose
γ_{mean}	0.26	0.24	0.24	0.25	0.21	-0.6%
$\gamma_{1\%}$	0.83	0.80	0.80	0.87	0.69	
$\% \gamma_{\leq 1}$	99.7	99.9	99.7	99.4	99.7	
Isoc -5cm						Δ Dose
γ_{mean}	0.27	0.26	0.23	0.25	0.21	-0.6%
$\gamma_{1\%}$	0.90	1.21	0.80	1.08	0.64	
$\% \gamma_{\leq 1}$	99.7	98.15	99.3	98.6	100	

X and Y profiles for the three depths (isocenter+5cm, isocenter and isocenter-5cm) are also plotted for each beam and presented in **Figure 2.6**.



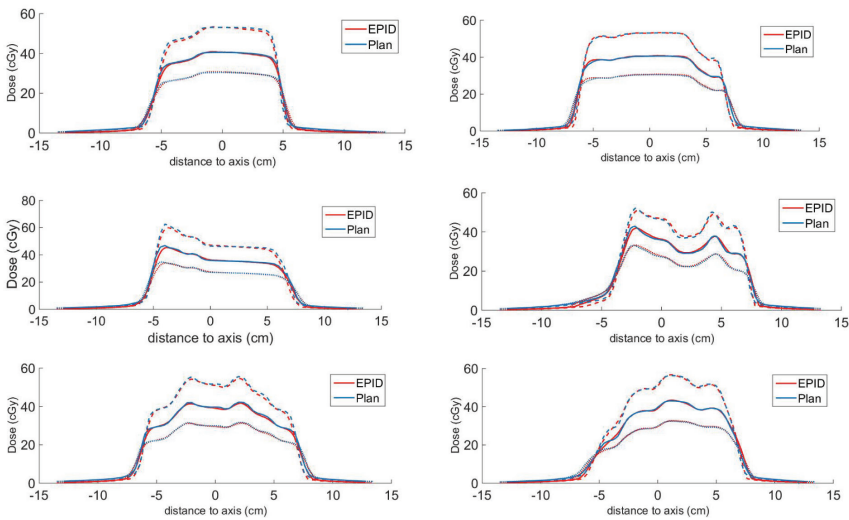


Figure 2.6: X-profiles are plotted in left column and Y-profiles in right column for each field (A-E). In dotted line the curve at isocenter-5cm, in solid the isocenter curve, and in dashed the isocenter+5cm curve.

In **Table 2.5** the γ parameters of the 2D γ -evaluation at the isocenter averaged over 58 IMRT fields are reported.

Table 2.5: γ -evaluation results (3%,3mm) averaged over the 58 IMRT fields. Our conventional algorithm was used to back-project portal images acquired without the aluminum structure (top) and our adapted algorithm to correct and back-project portal images acquired with the aluminum in place (bottom).

	γ_{mean}	$\gamma_{1\%}$	$\% \gamma_{\leq 1}$	$\Delta Dose_{iso}$ (cGy)
No-aluminum	0.28 ± 0.06	0.83 ± 0.15	99.5 ± 0.97	-0.80 ± 0.65
With aluminum	0.27 ± 0.06	0.91 ± 0.32	99.0 ± 1.3	-0.16 ± 0.90

2.4 Discussion

We have adapted our portal dosimetry algorithm to account for the presence of an MRI housing mock-up between patient and EPID in an MR-Linac system, that attenuates 72% and increases the scatter contribution of the EPID signal to 16%. The two new steps added to the conventional back-projection algorithm successfully corrected the portal dose images for the non-uniform attenuation between phantom (or patient) and EPID, and converted to the situation as if the MRI housing mock-up was not present. A complete back-projection of EPID images through the MRI mock-up was achieved, proving that the presence of an MRI scanner between patient and EPID in the MR-Linac should not become an impediment for the implementation of EPID dosimetry in the MR-Linac. The results presented in **Table 5** show that the performance of the adapted algorithm is similar to the conventional algorithm.

The accelerator where our experiments were performed at is equipped with an MLCi2 and the width of its leafs is 1 cm when projected at the isocenter. Because the commissioning of our algorithm was performed for field sizes not smaller than $2 \times 2 \text{ cm}^2$, the agreement of our EPID reconstructed profiles is less good for smaller fields sizes, such as in the area in which a single MCL leaf is open in the test field of **Figure 4.c**, where differences between the reconstructed EPID profile and the planned profile are up to 20%. This might yield to inaccuracies for highly modulated clinical fields, since results worsen the more, we differ from commissioning conditions. A commissioning including field sizes of $1 \times 1 \text{ cm}^2$ was not used because below $2 \times 2 \text{ cm}^2$, the field becomes smaller than the mini-phantom and the uncertainty in miniphantom setup increases considerably. Unwanted variations in $1 \times 1 \text{ cm}^2$ measurements may affect the results of the fit for larger field sizes, meaning that a fit to $1 \times 1 \text{ cm}^2$ data worsens the fit for larger field sizes.

Differences in linac energy, MLC design, and flattening filter between the linac where the experiments were carried out and the MR-Linac should not imply consequences in our reconstruction algorithm, since the original method has been used in our institute in linacs equipped with different MLC's, both with 6 and 10 MV and also FFF.

The scatter originated in the aluminum structure reaching the EPID is estimated via an on-axis fitting process for several field sizes, providing an accurate assessment of the scatter on axis but less precise off-axis. This is the cause of the wider penumbras in the EPID-derived profiles when compared to the TPS or microDiamond measured data. A better modelling of the scatter can only be achieved by a two-dimensional fitting procedure minimizing the distance between estimated scatter profiles and Monte Carlo simulated scatter profiles. We intend to apply this approach in the future adaptation of the algorithm for the real MR-Linac geometry. However, such Monte Carlo simulations were not performed for the aluminum mock-up.

Besides more sophisticated scatter modeling, other challenges will arise when we validate the proposed method in the real MR-Linac. The challenges for that are discussed next.

The calculations and measurements discussed in this paper were performed using a mock-up of the MR-Linac prototype geometry described by^{126, 93} and¹²⁴, which approximates the MRI housing on axis well. The actual design of the clinical MRL, however, has a smaller amount of material in the radiation beam causing less attenuation, scatter and beam hardening. The geometry of the more shielded areas (on the Y edges) has not been reported in literature and therefore the thickness of the thicker parts of our mock-up was chosen based on the values of EPID images acquired in the second MR-Linac prototype at UMC Utrecht. The reconstruction results for treatments with large field sizes (i.e. those exceeding 10 cm in the Y direction) demonstrate

that our adapted back-projection algorithm is able to reconstruct through these thicker parts.

Due to spatial constraints when mounting the aluminum mock-up between couch and EPID, for the verification of our IMRT plans the gantry was forced to be at 0° . Consequently, verification of VMAT plans could not be included in this study. However, in the actual MR-Linac and given its geometry, the beam will equally traverse the MRI scanner before hitting the EPID perpendicularly at any gantry angle. Therefore, the rotation of the gantry is not expected to alter the results of this study.

In contrast to the mock-up geometry, in the MR-Linac the beam will also traverse the MRI housing before reaching the patient. First of all, the influence of the MRI housing on the patient dose delivery will have to be taken care of in the TPS. Furthermore, the results of section 3.1 demonstrate that the scatter from the upper part of the aluminum mock-up is mostly absorbed by the lower aluminum structure, indicating that its effects on the EPID signal are limited. However, this is not relevant from the perspective of our algorithm, since empirical fits are performed to associate EPID pixel intensities to ionization chamber measurements. In other words, when an upper aluminum mock-up had been used for the commissioning of our model, similar results would have been expected. The extra the mock-up between source and isocenter was not included in the rest of the study to allow for straightforward comparison of EPID reconstructed and planned dose distributions.

The adapted method requires a set of commissioning data that includes EPID images and ionization chamber readings without the extra attenuating medium. While in this study the aluminum MR-Linac mock-up could easily be removed, the acquisition of these data in case of the MR-Linacs is less straightforward. Currently, we are

working on two approaches: the use of Monte Carlo simulations and measurements performed at an MR-Linac before the installation of the MRI scanner. Either of the two approaches are expected to provide sufficient information for a complete EPID dosimetric calibration for the MR-Linac.

2.5. Conclusion

Our EPID dosimetry back projection algorithm was successfully adapted for the presence of an extra step-shaped attenuating medium between phantom (or patient) and EPID. The aluminum MRI housing mock-up attenuates the beam by 72%, and causes 16% of the remaining EPID signal to consist of an extra scatter contribution. Experiments show excellent agreement between planned and EPID reconstructed dose distributions in a phantom positioned at the isocenter. This result is an essential step towards an accurate and independent dose verification tool for the MR-Linac.

2.6. Disclosure of conflicts of interest

Support for this research was provided, in part, by Elekta AB, Stockholm, Sweden.

2.7. Acknowledgments

We would like to thank Jan Kok, Job Geuze, Jochem Kaas, Thijs Perik and Begoña Vivas for assistance with the measurements.